

# Supporting Information

## Hollow MoC/NC Sphere for Electromagnetic Wave Attenuation: Direct Observation of Interfacial Polarization on nanoscale Hetero-interfaces

*Wenhuan Huang,<sup>ab\*</sup> Wenming Gao,<sup>ab</sup> Shouwei Zuo,<sup>b</sup> Luxi Zhang,<sup>a</sup> Ke Pei,<sup>c</sup> Panbo Liu<sup>c</sup> and Renchao Che,<sup>c\*</sup> Huabin Zhang,<sup>b\*</sup>*

<sup>a</sup>KAUST Catalysis Center, King Abdullah University of Science and Technology, 23955-6900, Thuwal, Kingdom of Saudi Arabia.

Email: huabin.zhang@kaust.edu.sa

<sup>b</sup>Key Laboratory of Chemical Additives for China National Light Industry, College of Chemistry and Chemical Engineering, Shaanxi University of Science and Technology, Xi'an 710021, China.

Email: huangwenhuan@sust.edu.cn

<sup>c</sup>Laboratory of Advanced Materials, Shanghai Key Lab of Molecular Catalysis and Innovative Materials, Fudan University, Shanghai 200438, P. R. China.

Email: rcche@fudan.edu.cn

### TABLE OF CONTENTS

<b>1 EXPERIMENTAL SECTION</b> .....	<b>1</b>
<b>2 CHARACTERIZATIONS</b> .....	<b>2</b>
<b>3 DATA ANALYSIS</b> .....	<b>3</b>
<b>4 RESULTS AND DISCUSSIONS</b> .....	<b>5</b>

**5 REFERENCES**.....**15**

## 1. Experimental Section

### 1.1 Synthesis of HZIF-ZnMo precursor

HZIF-ZnMo was synthesized on a typical procedure<sup>[1-2]</sup>. The mixture of  $\text{Zn}(\text{CH}_3\text{COO})_2 \cdot 2\text{H}_2\text{O}$  (5.28g, 24 mmol), 2-mim (2.88g, 36 mmol),  $\text{H}_2\text{MoO}_4$  (0.99 g, 6 mmol) and 120 ml DMF was kept stirring at 160°C for 6 hours in a 250ml round bottom flask. After a naturally cooling process, the white HZIF-ZnMo powder product obtained with the yield of 35%. The powder was then filtered and washed by ethanol for three times, and then dried at room temperature.

### 1.2 Synthesis of ZIF-Zn precursor

ZIF-Zn was synthesized on a typical procedure, according to the synthesis of ZIF-8<sup>[3]</sup>. The solution of  $\text{Zn}(\text{NO}_3)_2 \cdot 6\text{H}_2\text{O}$  (5.95 g, 20 mmol) in methanol (150 mL) was mixed with another solution of 2-mim (6.16 g, 75 mmol) in methanol (150 mL) and then fast stirred for 5 mins and kept in room temperature for 24 hours. As a result, the white ZIF-8 product (yield of 6.8 %) was filtered and washed by ethanol for three times, and then dried at room temperature.

### 1.3 Synthesis of H-HZIF-ZnMo and H-ZIF-Zn

HZIF-ZnMo and ZIF-Zn (0.3 g) powders were dispersed into the solution of 1.5 g tannic acid and 300 mL water, respectively, and then kept stirring for 10 mins. After that, the products of H-HZIF-ZnMo and H-ZIF-Zn were centrifuged and washed by water and ethanol separately for three times. After drying in vacuum oven at 60 °C for 3 hours, the 250 mg of earthy yellow H-HZIF-ZnMo and 240 mg of earthy yellow H-ZIF-Zn powder were obtained.

### 1.4 Synthesis of H-MoC/NC and H-NC

500 mg of above synthesized H-HZIF-ZnMo and H-ZIF-Zn were placed in corundum boats, respectively, and then heated to 900 °C through a rate of 8 °C/min at a tube furnace under the nitrogen

flow. After the keeping temperature at 900 °C for 2 hours, the samples were cooled down to room temperature naturally. The black powders of H-MoC/NC and H-NC were obtained.

### 1.5 Synthesis of MoC/NC and NC

As the contrast samples, the solid MoC/NC and NC were synthesized through the similar calcination process from the untreated HZIF-ZnMo and ZIF-Zn precursors (products in 1.1 and 1.2 steps).

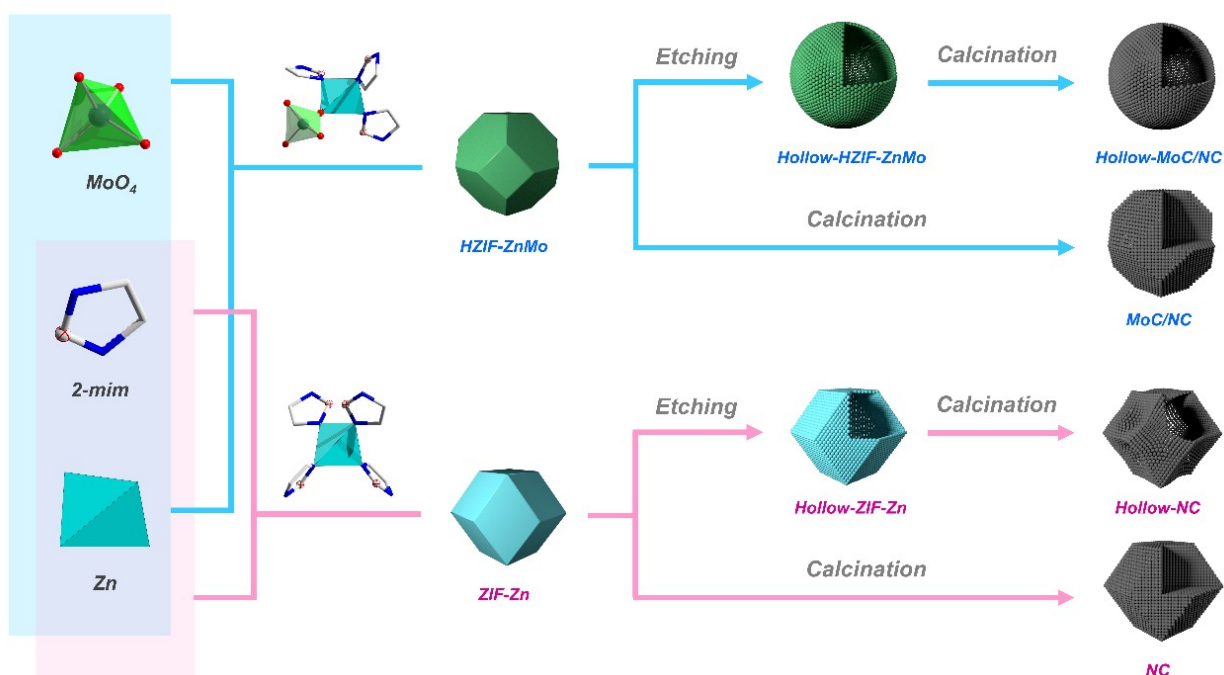


Figure S1. The scheme of the synthesis routes for all the samples in this work.

## 2. Characterizations

D8 DAVANCI X-ray powder diffractometer equipped with graphite monochromatized Cu K $\alpha$  radiation ( $\lambda = 0.1542$  nm) was used to record powder X-ray diffraction (PXRD) patterns in the  $2\theta$  range of 5°-80° with a scanning rate of 1 °/min. The specific surface area was measured by nitrogen adsorption and desorption at 77 K by ASAP 2020 sorption system. Scanning electron microscopy (SEM) images were collected by a Hitachi S4800 apparatus with an acceleration voltage of 2 kV. The transmission electron microscopy (TEM) images were recorded on a JEM-2010HR apparatus working at an accelerating voltage of 200 kV and X-ray energy-dispersive spectroscopy (EDS) was taken on a

JEM-2010HR-Vantage typed energy spectrometer. X-ray photoelectron spectroscopy (XPS) was implemented on Thermo ESCA Lab250XI. The surface area (BET) of the samples was measured by N<sub>2</sub> adsorption and desorption at 77K using an ASAP 2020 sorption system. Raman spectroscopy of the samples was obtained by a Renishaw in Via Raman Microscope. The electromagnetic parameters were analyzed using a HP8753D vector network analyzer in the frequency range of 2-18 GHz. The measured samples were dispersed in paraffin homogeneously with a sample-to-paraffin weight ratio of 3:17, and then the mixture was pressed into a toroidal shape with an inner diameter of 2.0 mm and an outer diameter of 7.0 mm. The conductivity of the samples (1 cm × 1 cm) was performed through a ST2253 four-probe resistance meter.

### 3. Data analysis

Cole–Cole semicircle model (Equation S1):

$$\left(\varepsilon' - \frac{\varepsilon_s + \varepsilon_\infty}{2}\right)^2 + (\varepsilon'')^2 = \left(\frac{\varepsilon_s - \varepsilon_\infty}{2}\right)^2 \quad (\text{Equation S1})$$

Each semicircle in the  $\varepsilon'$ – $\varepsilon''$  curve stands for a polarization relaxation process. The  $\varepsilon_s$  and  $\varepsilon_\infty$  represent the static dielectric constant, the dielectric constant at infinite frequency, respectively. The high number of semicircles means the strong dipole polarization process.

Debye relaxation correction formula (Equation S2-3):

$$\varepsilon_r = \varepsilon_{r\infty} + \frac{\varepsilon_{rs} - \varepsilon_{r\infty}}{1 + (i\omega\tau)^{1-A}} \quad (0 < A < 1) \quad (\text{Equation S2})$$

$$\varepsilon_r' = \varepsilon_{r\infty} + (\varepsilon_{rs} - \varepsilon_{r\infty}) \frac{1 + (\omega\tau)^{(1-A)} \sin \frac{\pi A}{2}}{1 + 2(\omega\tau)^{1-A} \sin \frac{\pi A}{2} + (\omega\tau)^{2(1-A)}} \quad (\text{Equation S3})$$

$\varepsilon_p''$  and  $\varepsilon_c''$  are the dielectric loss contributed by polarization relaxation and charge transport, respectively, which can be obtained according to Debye theory (Equation S4-6).

$$\varepsilon_c'' = \frac{\sigma}{2\pi f \varepsilon_0} \quad (\text{Equation S4})$$

$$\varepsilon_p'' = \frac{\varepsilon_s - \varepsilon_\infty}{1 + (2\pi f)^2 \tau^2} \omega \tau = \varepsilon'' - \varepsilon_c'' \quad (\text{Equation S5})$$

$$\varepsilon'' = \frac{\varepsilon_s - \varepsilon_\infty}{1 + (2\pi f)^2 \tau^2} \omega \tau + \frac{\sigma}{2\pi f \varepsilon_0} = \varepsilon_p'' + \varepsilon_c'' \quad (\text{Equation S6})$$

Where  $\varepsilon_s$  is the relative permittivity at static, and  $\varepsilon_\infty$  is that at “infinite” high frequency.  $\sigma$  is the conductivity, Conductivity is a parameter used to describe the difficulty of charge flow in matter.

The attenuation coefficient ( $\alpha$ ):

$$\alpha = \frac{\sqrt{2\pi f}}{c} \sqrt{(\mu'' \varepsilon'' - \mu' \varepsilon') + \sqrt{(\mu'' \varepsilon'' - \mu' \varepsilon')^2 + (\mu' \varepsilon'' + \mu'' \varepsilon')^2}} \quad (\text{Equation S7})$$

The reflection loss ( $R_L$ ) values of the absorbers are calculated according to transmission line theory by the following equation S8-9:

$$R_L(\text{dB}) = 20 \lg \left| \frac{Z_{in} - Z_0}{Z_{in} + Z_0} \right| \quad (\text{Equation S8})$$

$$Z_{in} = Z_0 \sqrt{\frac{\mu_r}{\varepsilon_r}} \tanh \left[ j \left( \frac{2\pi f d}{c} \right) \sqrt{\mu_r \varepsilon_r} \right] \quad (\text{Equation S9})$$

Where  $Z_0$  is the characteristic impedance of free space,  $Z_{in}$  is the normalized input impedance of absorber,  $\varepsilon_r$  and  $\mu_r$  are the relative complex permittivity and permeability,  $d$  is the layer thickness,  $c$  is the speed of light in free space and  $f$  is the frequency.

The absorption peak shifts toward low frequency with increasing the thickness, which can be explained by Equation S10 according to quarter-wavelength matching model:

$$d_m = \frac{n\lambda}{4} = \frac{nc}{4f_m \sqrt{|\varepsilon_r| |\mu_r|}} \quad (n = 1, 3, 5, \dots) \quad (\text{Equation S10})$$

The  $d_m$  and  $f_m$  in the equation represent the matching thickness and the matching frequency, respectively. The interference effect between the reflected and incident microwave will result in the microwave energy dissipation when the  $d_m$  and  $f_m$  value accords with Equation S10.

#### 4. Results and discussions

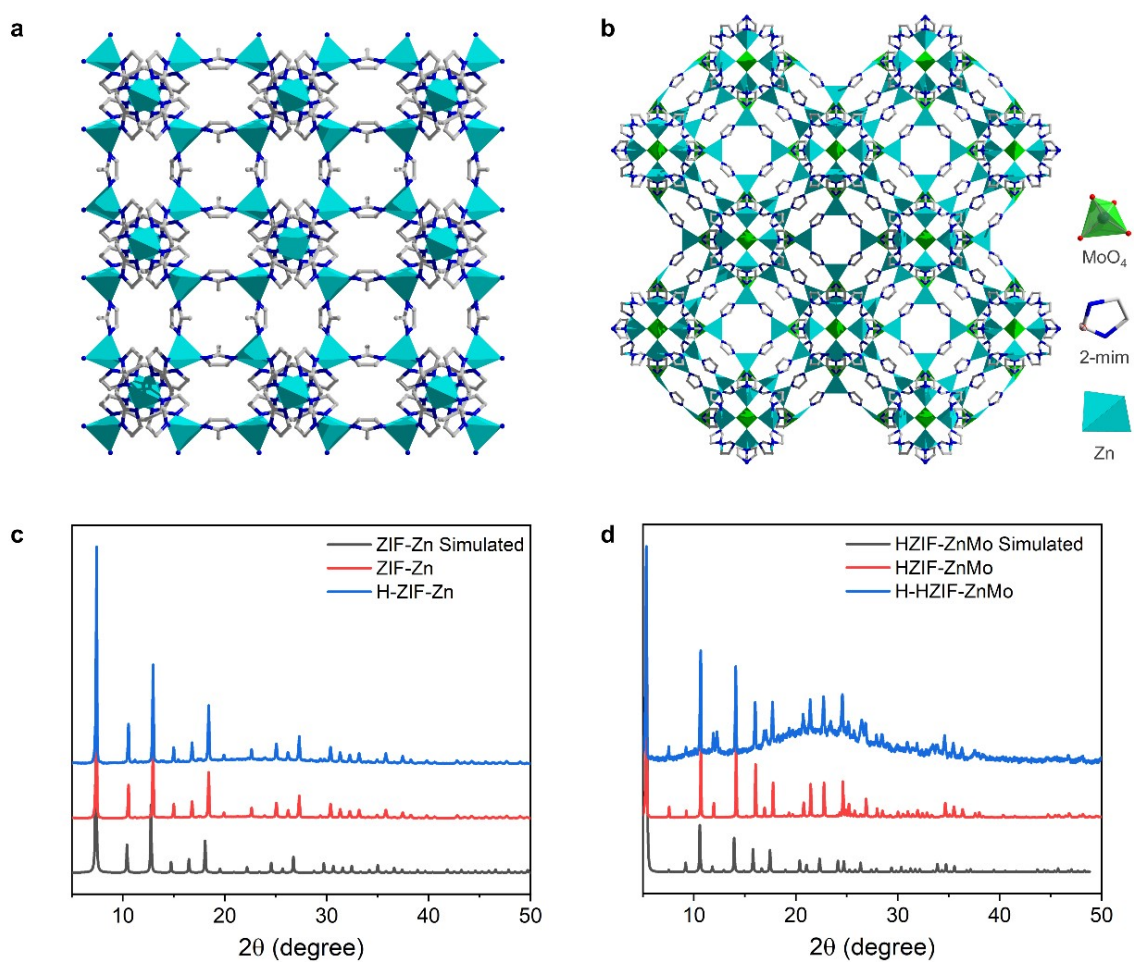


**Figure S2.** The crystalline structure of ZIF-Zn (a) and HZIF-ZnMo (b), the PXRD results of synthesized ZIF-Zn and H-ZIF-Zn (c), HZIF-ZnMo and H-HZIF-ZnMo (d).

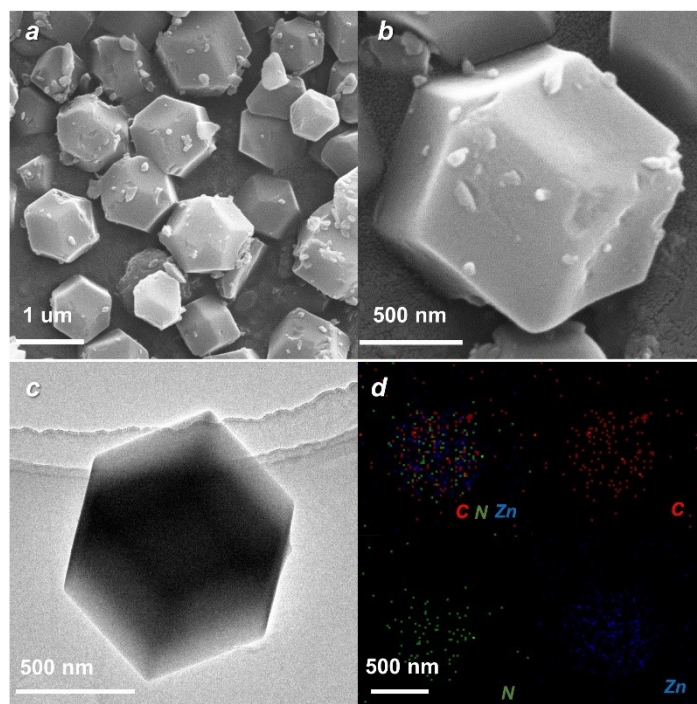


**Figure S3.** The SEM (a-b), TEM (c) and the TEM-EDS mapping (d) of ZIF-Zn.

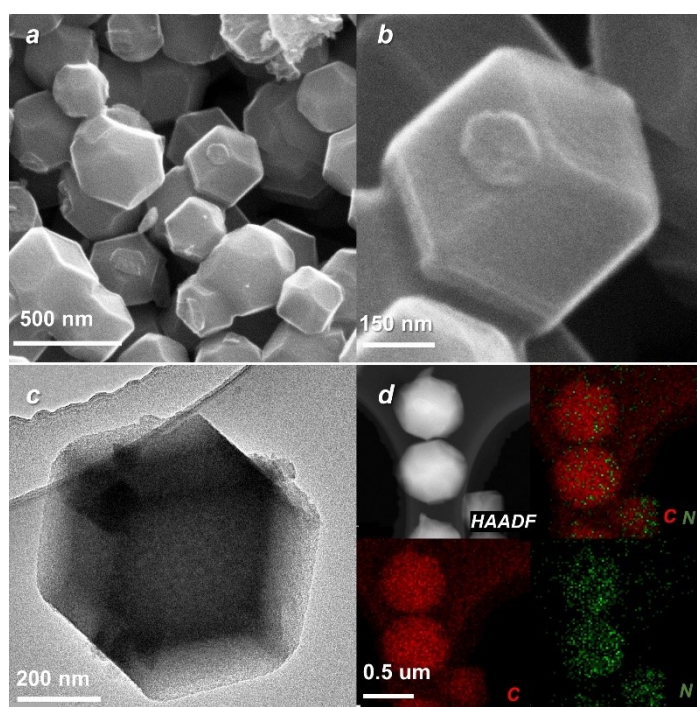


**Figure S4.** The SEM (a-b), TEM (c) and the TEM-EDS mapping (d) of NC.



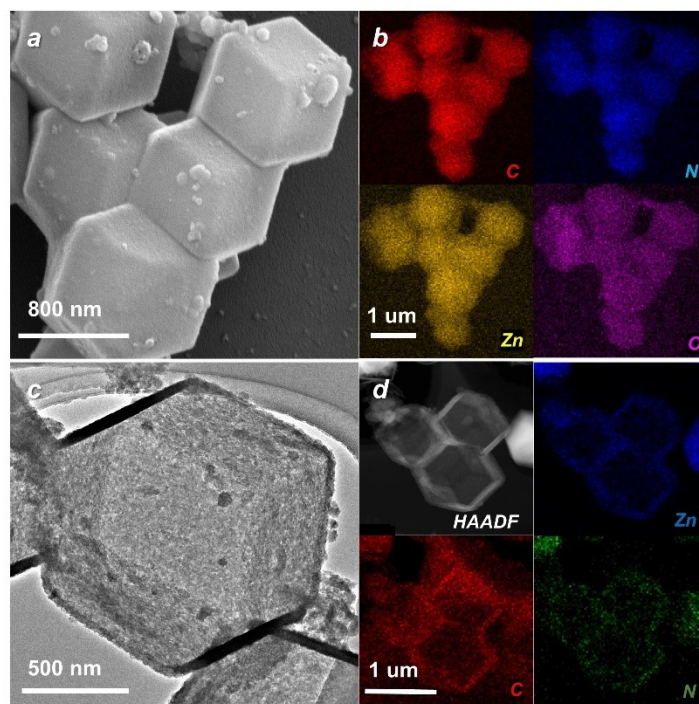


**Figure S5.** The SEM (a), SEM-EDS mapping (b), TEM (c) and the TEM-EDS mapping (d) of H-ZIF-Zn.

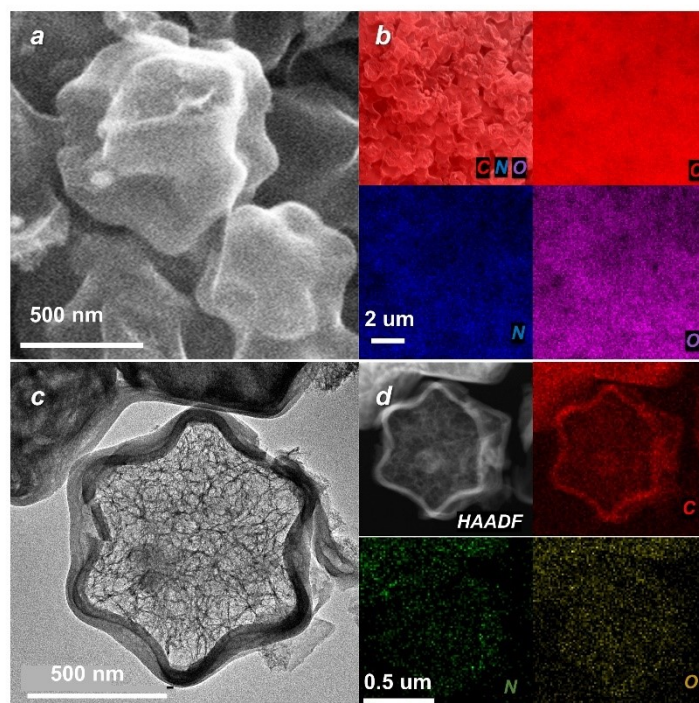


**Figure S6.** The SEM (a), SEM-EDS mapping (b), TEM (c) and the TEM-EDS mapping (d) of H-NC.

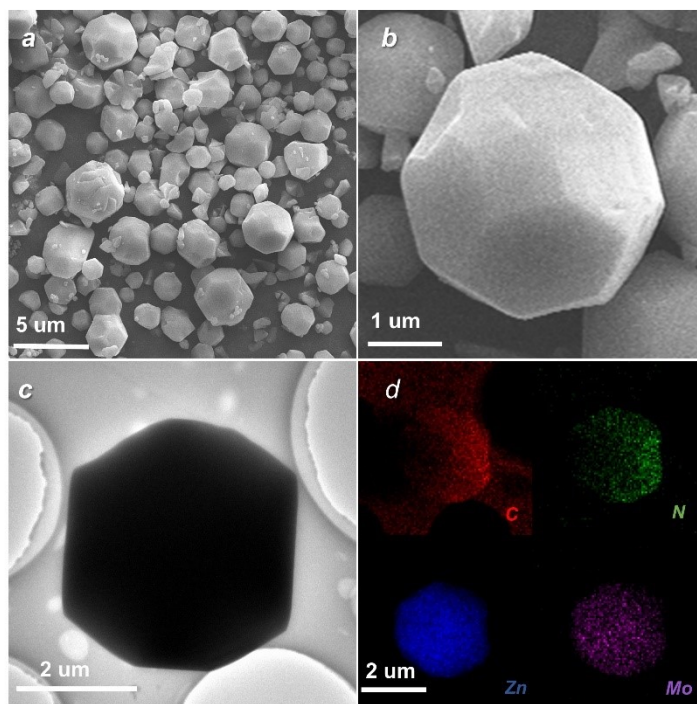


**Figure S7.** The SEM (a-b), TEM (c) and the TEM-EDS mapping (d) of HZIF-ZnMo.

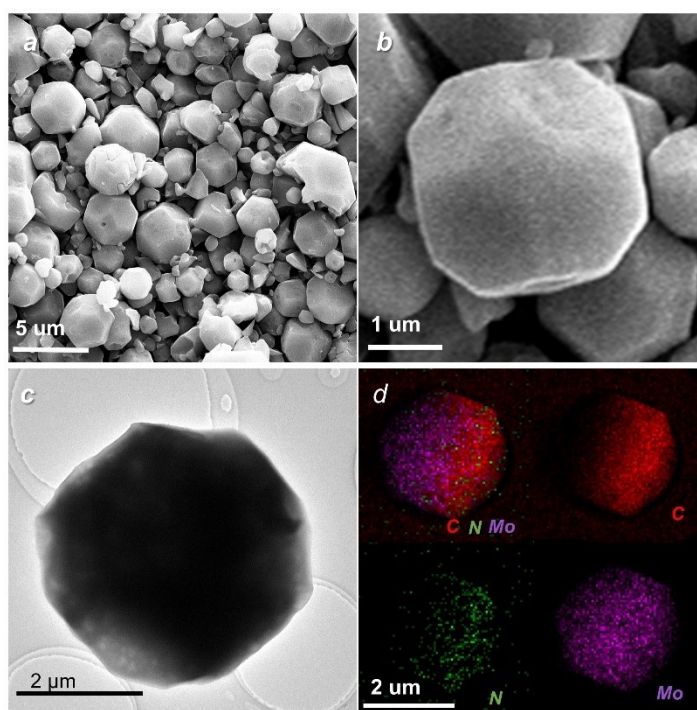


**Figure S8.** The SEM (a-b), TEM (c) and the TEM-EDS mapping (d) of MoC/NC.

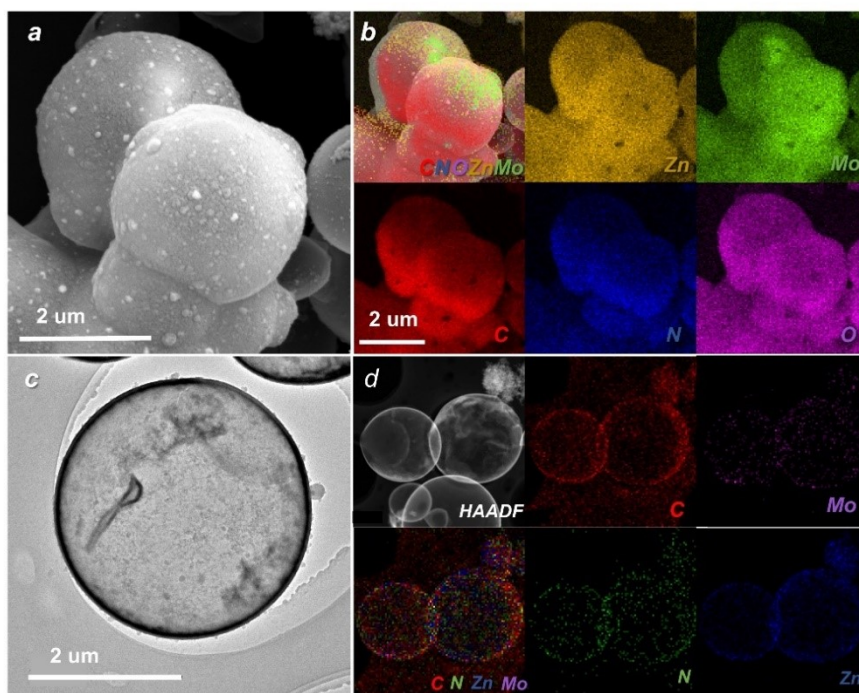


**Figure S9.** The SEM (a), SEM-EDS mapping (b), TEM (c) and the TEM-EDS mapping (d) of H-ZIF-ZnMo.

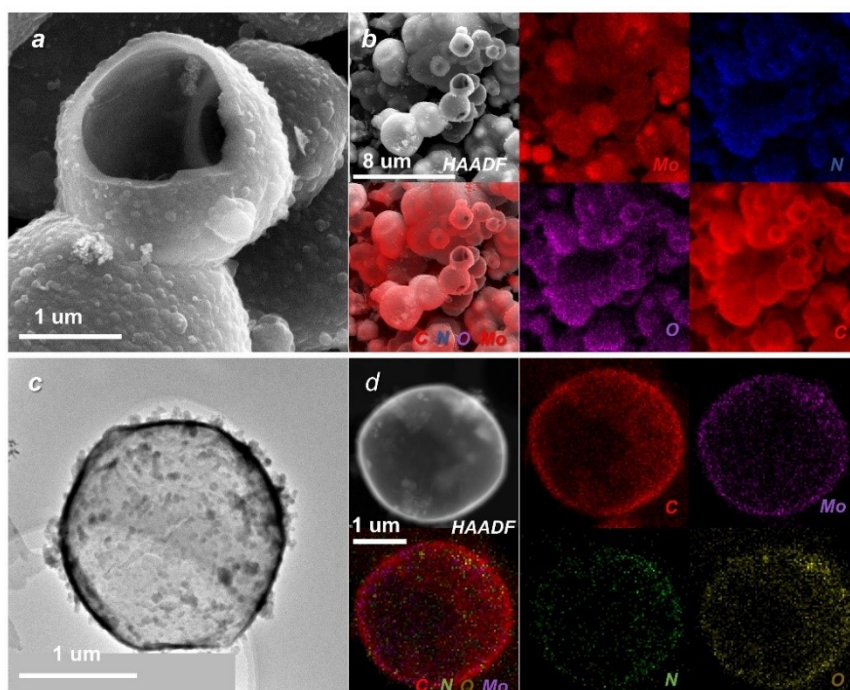


**Figure S10.** The SEM (a), SEM-EDS mapping (b), TEM (c) and the TEM-EDS mapping (d) of H-MoC/NC.

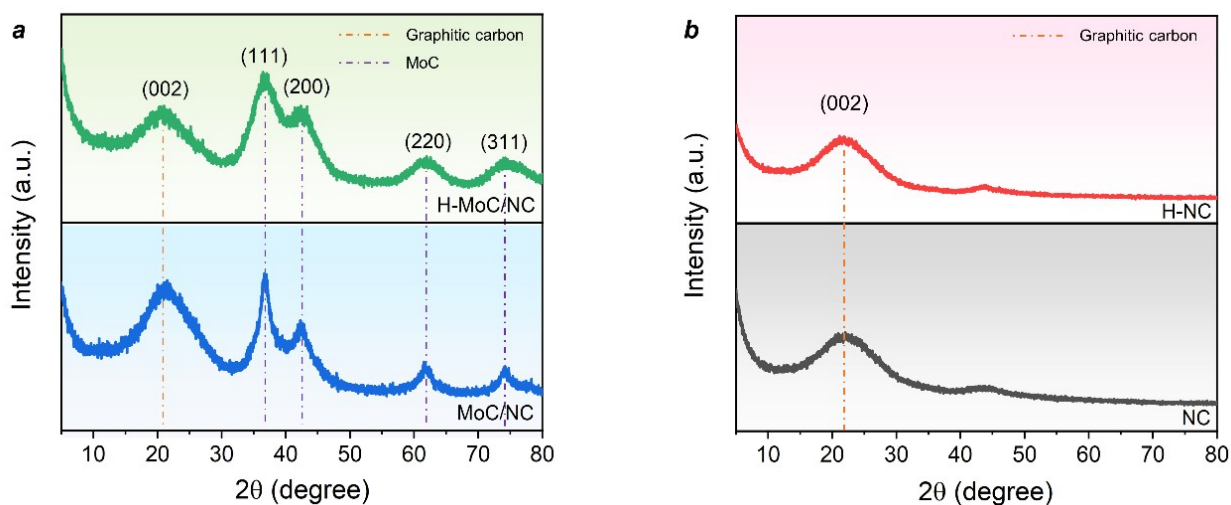


**Figure S11.** The PXRD of the MoC/NC (blue), H-MoC/NC (green), and NC (black), H-NC (red).

The PDF card for  $\alpha$ -MoC is JCPDS-01-089-2868.

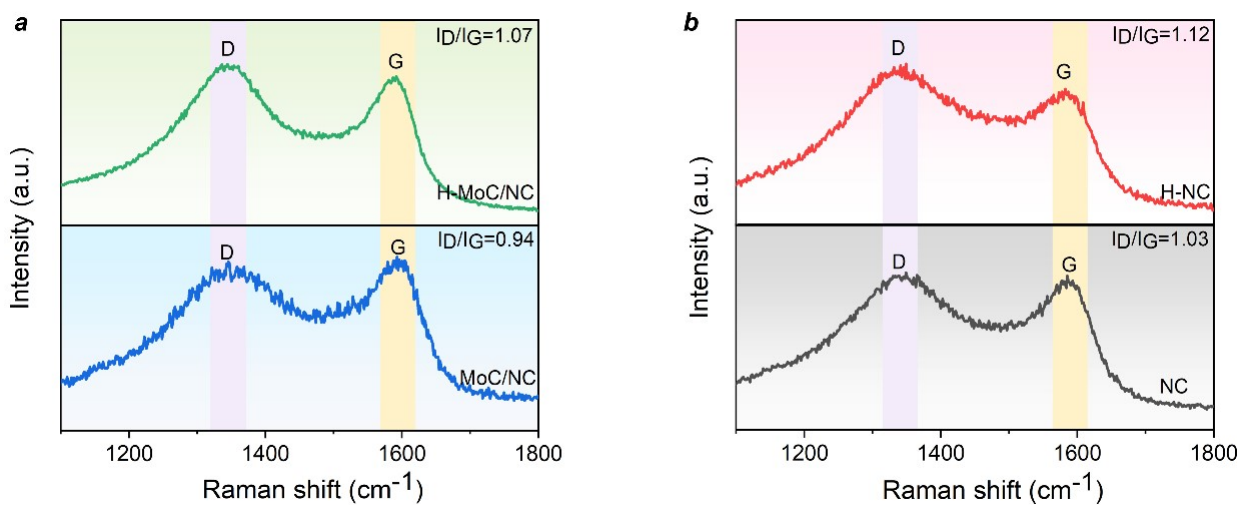


**Figure S12.** The Raman spectrum of the MoC/NC (blue), H-MoC/NC (green), and NC (black), H-NC (red). Peaks of D band and G band lie at  $1350 \text{ cm}^{-1}$  and  $1590 \text{ cm}^{-1}$ .

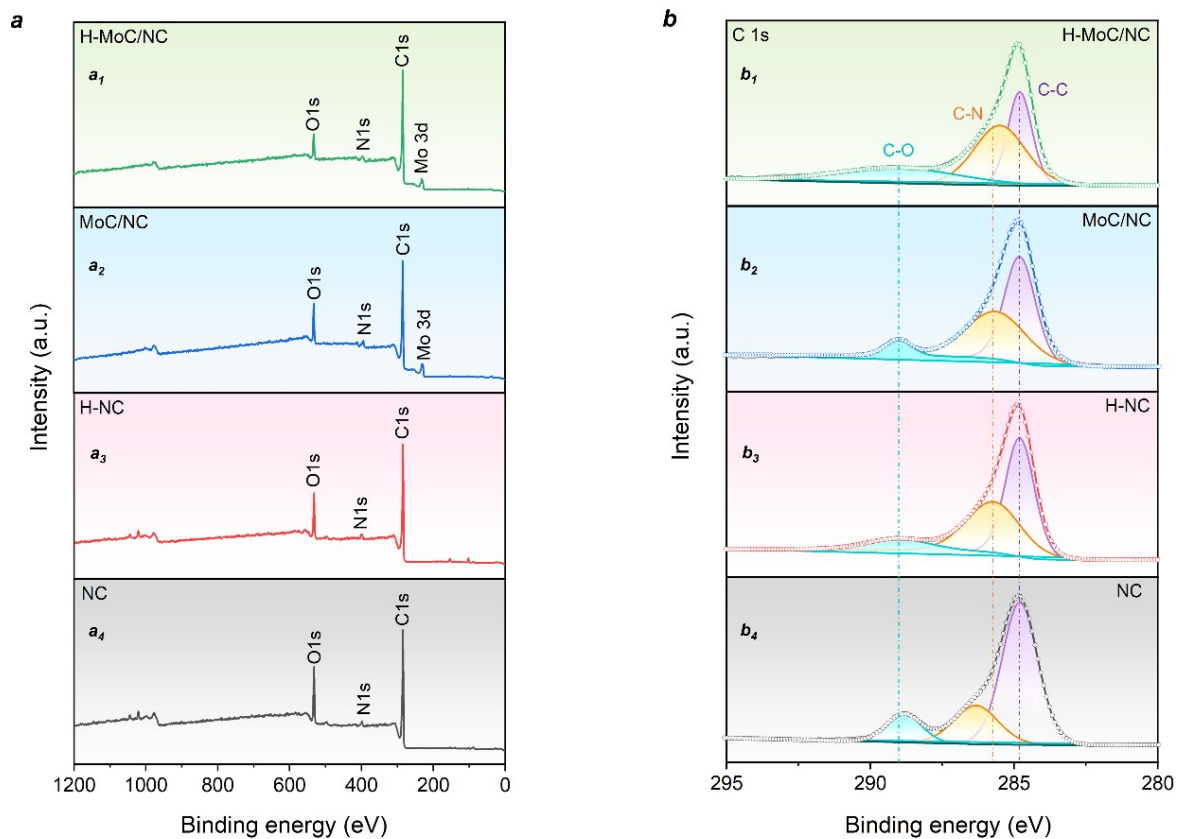


**Figure S13.** The survey XPS spectrum (a) of H-MoC/NC, MoC/NC, H-NC and NC. The XPS spectra of C 1s (b), spectrum in H-MoC/NC, MoC/NC, H-NC and NC.

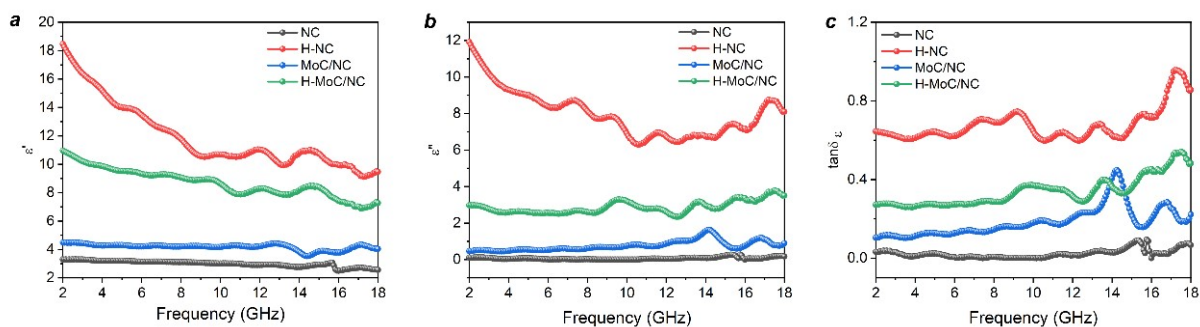


**Figure S14.** The real part of permittivity (a), imaginary part of permittivity (b), dielectric loss tangent (c) of H-MoC/NC, MoC/NC, H-NC and NC.

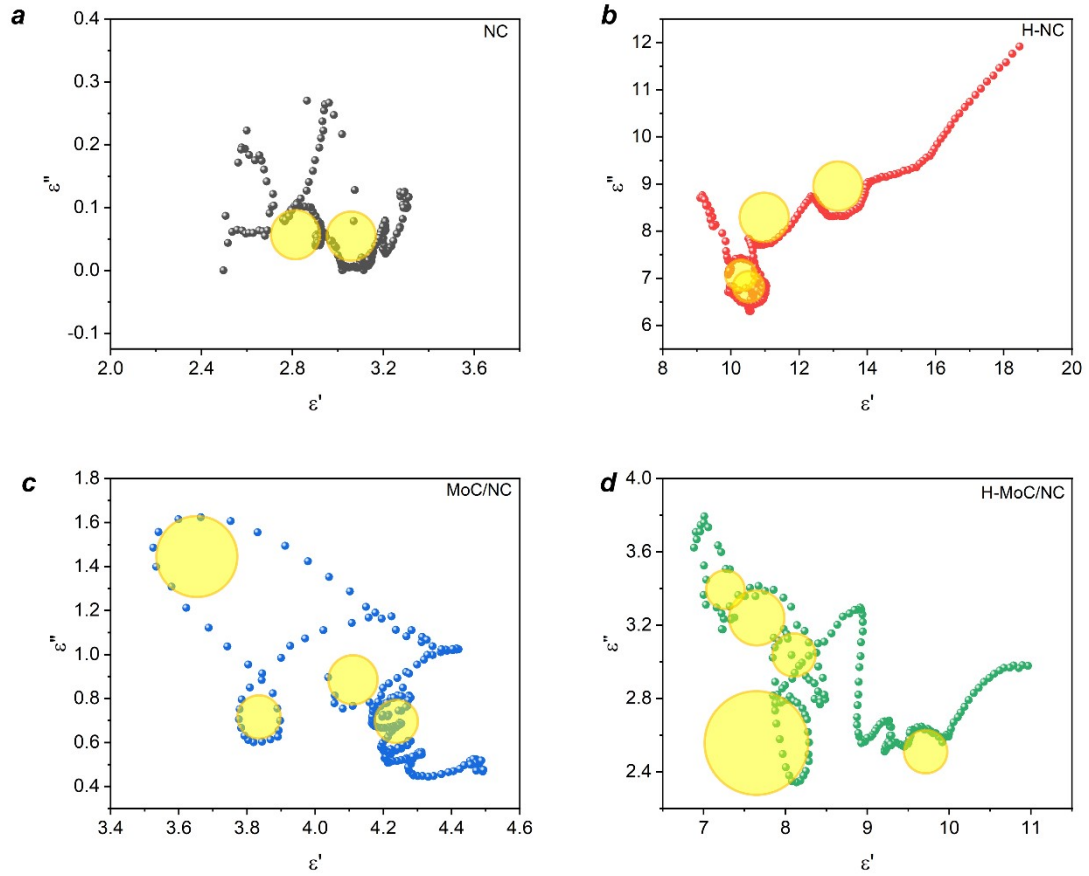


**Figure S15.** The Cole-Cole curves of H-MoC/NC, MoC/NC, H-NC and NC.

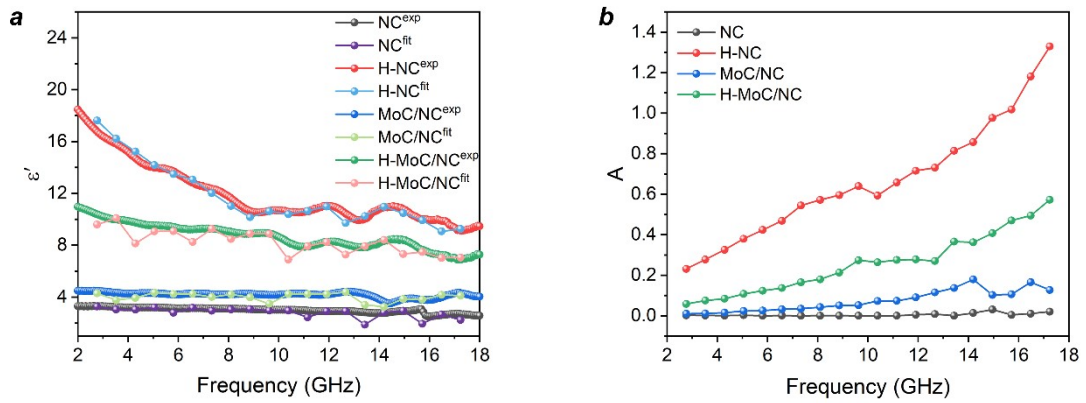


**Figure S16.** Real part of permittivity of measured and empirical formula fitted of of NC, H-NC, MoC/NC, H-MoC/NC (a). The interface factor A values of NC, H-NC, MoC/NC, H-MoC/NC (b).

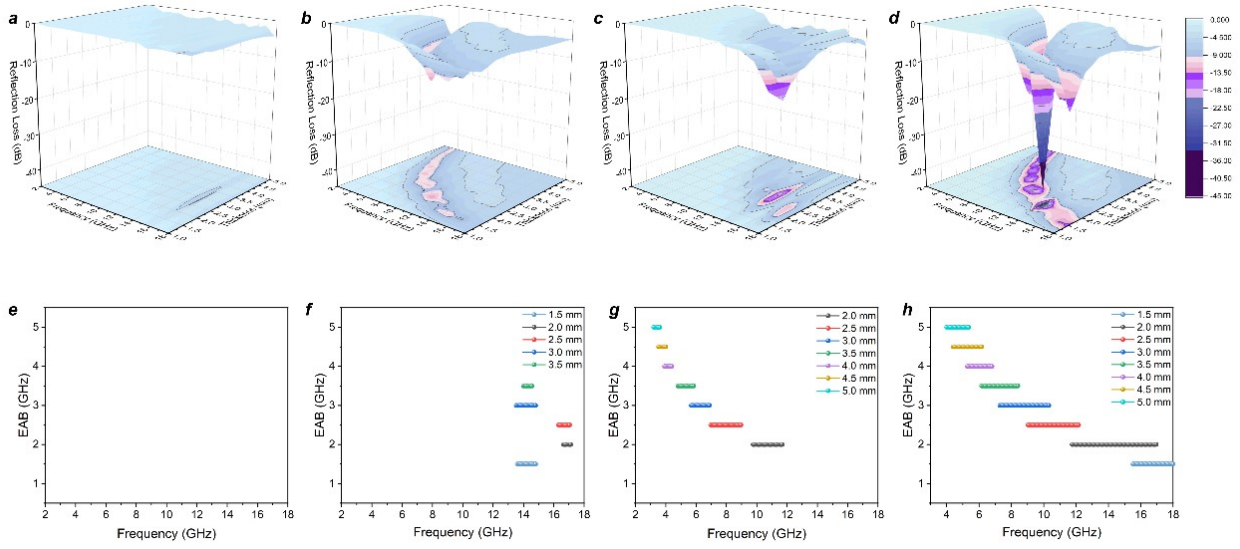


**Figure S17.** The 3D RL and the effective frequency bandwidth (RL < -10 dB) of NC (a, e), H-NC (b, f), MoC/NC (c, g), H-MoC/NC (d, h).

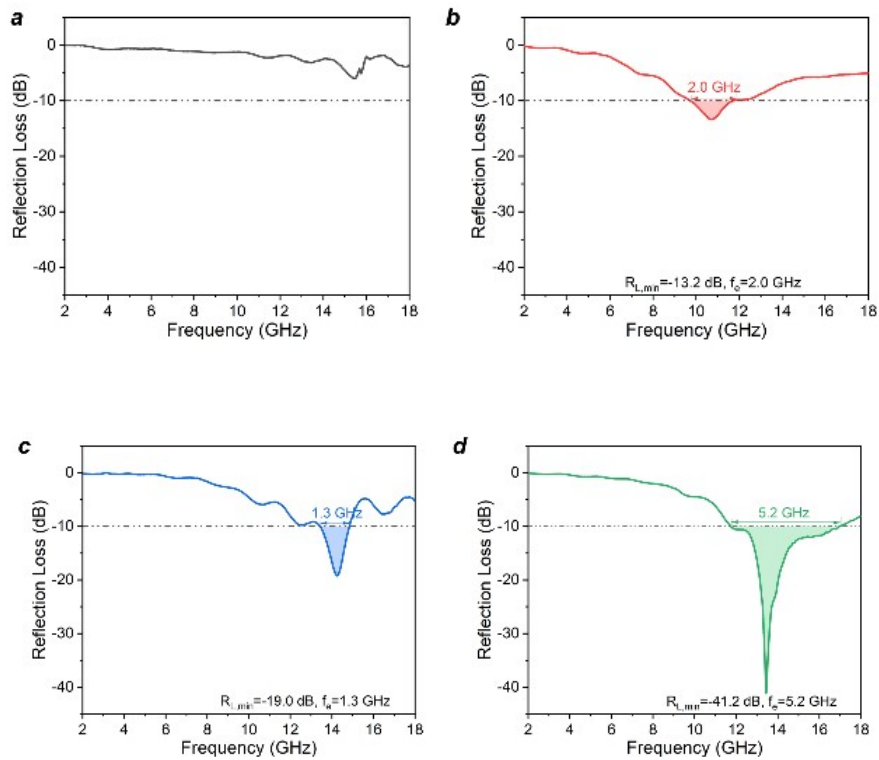


**Figure S18.** The best of  $R_L$  values and the effective frequency bandwidth (RL < -10 dB) of NC (a), H-NC (b), MoC/NC (c), H-MoC/NC (d).

Table S1. Comparison of microwave absorption performance of H-MoC/NC with other MOFs-derived carbon absorbers.

Absorber	$R_L$ (dB)	Thickness (mm)	Range (<10 GHz)	$e_f$ (GHz)	Loading (wt %)	$SR_L$	Ref.
ZnFe <sub>2</sub> O <sub>4</sub> @C@MoS <sub>2</sub> /FeS <sub>2</sub>	-52.50	2.23	10.10-15.08	4.98	35%	-150	10
MoS <sub>2</sub> @M <sub>x</sub> -2	-51.00	4.00	6.00-10.80	4.80	30%	-170	11
Al@MoS <sub>2</sub> /rGO	-33.38	1.30	25.42-29.18	3.76	35%	-95	12
MoS <sub>2</sub> @C	-56.97	5.00	12.56-18.00	5.44	35%	-163	13
MSCF8	-45.88	2.20	8.20-13.82	5.62	35%	-131	14
PPy@MoS <sub>2</sub>	-49.10	2.50	11.50-17.50	6.10	40%	-123	15
MoS <sub>2</sub> /Fe@Fe <sub>3</sub> O <sub>4</sub>	-31.80	1.52	13.20-18.00	4.80	35%	-91	16
CoS <sub>2</sub> @MoS <sub>2</sub> -2	-31.12	3.10	14.85-17.21	2.36	35%	-89	17
Co <sub>x</sub> S <sub>y</sub> /C@MoS <sub>2</sub>	-41.32	3.30	7.24-10.91	3.67	35%	-118	17
Mo <sub>2</sub> C/C	-49.19	2.60	8.00-11.96	3.96	20%	-246	18
H-MoC/NC	-41.20	2.00	11.76-16.96	5.20	15%	-275	This Work

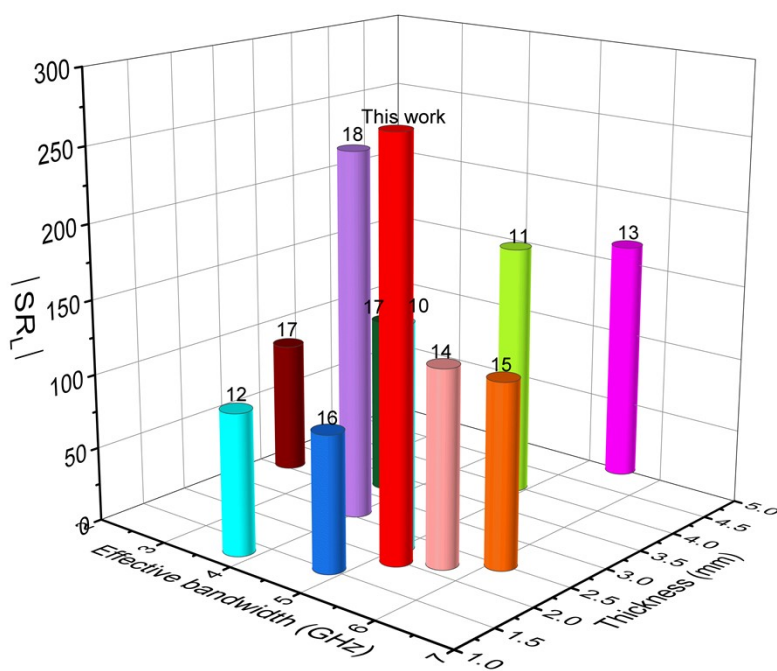
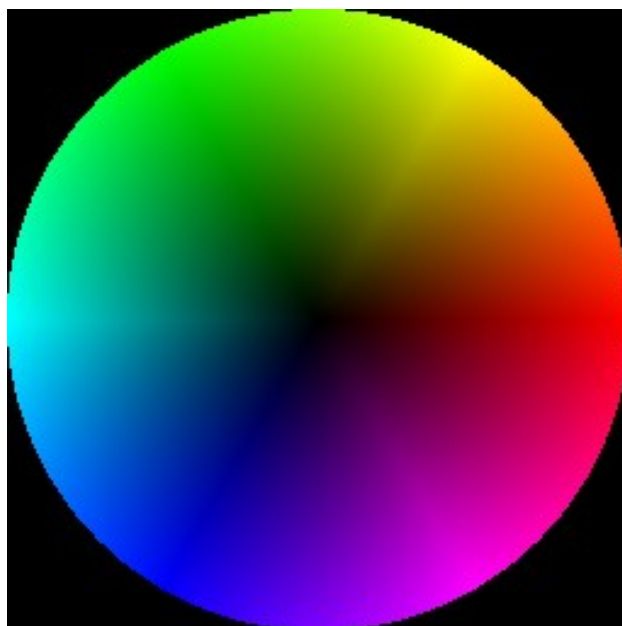


Figure S19. EMW absorption performance of Mo-based materials: comparison of  $SR_L$  (ratio of  $RL$ /loading amount), effective bandwidth and thickness.





**Figure S20.** The colour disk for electric field distribution diagram, colour represents direction and brightness represents intensity.

## 5. References

1. F. Wang, Z. S. Liu, H. Yang, Y. X. Tan, and J. Zhang, Hybrid zeolitic imidazolate frameworks with catalytically active TO4 building blocks. *Angew. Chem. Int. Ed.*, 2011, 50(2): 450-453.
2. P. Liu, S. Gao, W. Huang, J. Ren, D. Yu, and W. He, Hybrid zeolite imidazolate framework derived N-implanted carbon polyhedrons with tunable heterogeneous interfaces for strong wideband microwave attenuation. *Carbon*, 2020, 159: 83-93.
3. Park, K.; Ni, Z.; Côté, A.; Choi, J.; Huang, R.; Uribe-Romo, F.; Chae, H.; O'Keeffe, M.; Yaghi, O. *Proceedings of the National Academy of Sciences* 2006, 103(27), 10186-10191.
4. Pan F, et al. Lotus Leaf-Derived Gradient Hierarchical Porous C/MoS<sub>2</sub> Morphology Genetic Composites with Wideband and Tunable Electromagnetic Absorption Performance. *Nano-Micro Letters* 13, (2021).
5. X. Yan, X. Huang, Z. Bo, W. Tong, H. Wang et al., Balancing interface polarization strategy for enhancing electromagnetic wave absorption of carbon materials. *Chem. Eng. J.* 391, 123538 (2020).
6. H.Wang, F.Meng, F.Huang, C. Jing, Y. Li et al., Interface modulating CNTs@PANI hybrids by controlled unzipping of the walls of cnts to achieve tunable high-performance microwave absorption. *ACS Appl. Mater. Interfaces* 11, 12142– 12153 (2019).
7. X. Li, E. Cui, Z. Xiang, L. Yu, J. Xiong et al., Fe@NPC@CF nanocomposites derived from Fe-MOFs/biomass cotton for lightweight and high-performance electromagnetic wave absorption applications. *J. Alloys Compd.* 819, 152952 (2020).

8. E. Cui, F. Pan, Z. Xiang, Z. Liu, L. Yu, et al., Engineering dielectric loss of FeCo/polyvinylpyrrolidone core-shell nanochains@graphene oxide composites with excellent microwave absorbing properties. *Adv. Eng. Mater.* 2000827 (2020).
9. S. Wang, S. Peng, S. Zhong, W. Jiang, Construction of SnO<sub>2</sub>/Co<sub>3</sub>Sn<sub>2</sub>@C and SnO<sub>2</sub>/Co<sub>3</sub>Sn<sub>2</sub>@air@C hierarchical heterostructures for efficient electromagnetic wave absorption. *J. Mater. Chem. C* 6, 9465–9474 (2018).
10. Liao Z, et al. Fabrication of one-dimensional ZnFe<sub>2</sub>O<sub>4</sub>@carbon@MoS<sub>2</sub>/FeS<sub>2</sub> composites as electromagnetic wave absorber. *J Colloid Interface Sci* 600, 90-98 (2021).
11. Hassan A, et al. Modulating dielectric loss of MoS<sub>2</sub>@Ti<sub>3</sub>C<sub>2</sub>T<sub>x</sub> nanoarchitectures for electromagnetic wave absorption with radar cross section reduction performance verified through simulations. *Ceramics International* 47, 20706-20716 (2021).
12. Prasad J, Singh AK, Tomar M, Gupta V, Singh K. Hydrothermal synthesis of micro-flower like morphology aluminum-doped MoS<sub>2</sub>/rGO nanohybrids for high efficient electromagnetic wave shielding materials. *Ceramics International* 47, 15648-15660 (2021).
13. Ye S, et al. Carbon encapsulation of MoS<sub>2</sub> nanosheets to tune their interfacial polarization and dielectric properties for electromagnetic absorption applications. *Journal of Materials Chemistry C* 9, 537-546 (2021).
14. Lyu L, et al. Constructing 1T/2H MoS<sub>2</sub> nanosheets/3D carbon foam for high-performance electromagnetic wave absorption. *J Colloid Interface Sci* 586, 613-620 (2021).
15. Gai L, et al. Construction of core-shell PPy@MoS<sub>2</sub> with nanotube-like heterostructures for electromagnetic wave absorption: Assembly and enhanced mechanism. *Composites Part A: Applied Science and Manufacturing* 136, (2020).
16. Wang P, et al. Synthesis and characterization of MoS<sub>2</sub>/Fe@Fe<sub>3</sub>O<sub>4</sub> nanocomposites exhibiting enhanced microwave absorption performance at normal and oblique incidences. *Journal of Materials Science & Technology* 35, 1931-1939 (2019).
17. Zhu Q, et al. Co<sub>x</sub>S<sub>y</sub>/C@MoS<sub>2</sub> nanofibers: synthesis, characterization and microwave absorption investigation. *Journal of Materials Science: Materials in Electronics*, (2020).
18. Dai S, et al. Porous-carbon-based Mo<sub>2</sub>C nanocomposites as excellent microwave absorber: a new exploration. *Nanoscale* 10, 6945-6953 (2018).